Role of Seepage Forces on Seismicity Triggering

1 author:

Role of seepage forces on seismicity triggering

Alexander Y. Rozhko[1]

[1]   Borehole fluid injection is commonly used for geological sequestration of carbon dioxide, underground storage of natural gas, waste injections, and during stimulations and development of geothermal and hydrocarbon reservoirs. Typically, the injection process induces significant seismicity, with some earthquakes as large as magnitude four. Induced seismicity has also been observed around producing hydrocarbon boreholes. Recently, it has been argued that some induced seismicity data can be explained by a highly nonlinear fluid diffusion mechanism or by the propagation of fluid pressure pulses. The nature of the nonlinearity and the mechanisms by which a pressure pulse can trigger seismicity are still uncertain. In this paper I show that the same spatiotemporal variation of seismicity can be explained and predicted by linear diffusion coupled to deformation of a linear poroelastic medium. By calculating the propagation of Coulomb Yielding Stress (CYS) perturbation with time, it is demonstrated that seismicity can be triggered by this perturbation. The change of CYS along the diffusion front is caused by seepage forces, which are body forces generated by fluid pressure gradients, and can explain induced seismicity during borehole fluid injection and extraction. Using published experimental data, I demonstrate how the spatiotemporal distribution of fluid-induced seismic events can be used for reservoir modeling and characterization.

1. Introduction

[2] Seismicity triggering/quiescence is a process by which stress change associated with a causative event can promote/ suppress seismic activity in the surroundings [*Stein*, 1999; *Freed*, 2005]. The calculation of Coulomb Failure Stress (CFS) transfer associated with earthquake slip has proven to be a powerful tool in explaining many seismological observations [*Stein*, 1999; *Freed*, 2005]. The CFS is based on the Mohr-Coulomb failure criterion, controlling the shear failure, which on an optimally oriented fault can be written as follows [*Paterson and Wong*, 2005]:

$$CFS = \frac{\sigma_1 - \sigma_3}{2} + \sin\varphi\left(\frac{\sigma_1 + \sigma_3}{2} + p_f\right) + C\cos\varphi, \quad (1)$$

where σ_1 and σ_3 are the maximum and minimum principal stresses, negative in compression; p_f is the fluid pressure; φ is the angle of internal friction; and C is the cohesion. The rock is stable if $CFS < 0$ and unstable if $CFS = 0$. The change in CFS associated with a causative event is calculated as

$$\Delta CFS = \Delta\tau + (\Delta\sigma_m + \Delta p_f)\sin\varphi, \quad (2)$$

where $\Delta\tau$, $\Delta\sigma_m$, and Δp_f are perturbations of the Mohr's circle radius ($\tau = \frac{\sigma_1 - \sigma_3}{2} = \sqrt{(\sigma_{11} - \sigma_{33})^2/4 + \sigma_{13}^2}$), mean stress ($\sigma_m = \frac{\sigma_1 + \sigma_3}{2} = \frac{\sigma_{11} + \sigma_{33}}{2}$), and pore fluid pressure, respectively. The physical meaning of CFS is the proximity to failure. If $\Delta CFS > 0$, the proximity to failure is increased, and if $\Delta CFS < 0$, the proximity to failure is decreased.

[3] Laboratory experimental results show that the onset of marked acoustic emissions during triaxial loading of the samples is well correlated with the onset of dilatancy [*Scholz*, 1968; *Barron*, 1971; *Fortin et al.*, 2009]. Dilatancy is a nonelastic response caused by microfracturing of rock material, and is described as material yielding [e.g., *Paterson and Wong*, 2005]. The onset of dilatancy can be defined as the point at which the observed instantaneous Poisson's ratio exceeds 0.5 [*Sangha and Dhir*, 1975; *Paterson and Wong*, 2005], with typical differential stress levels between one-third and two-thirds of the macroscopic fracture (failure) stress. In some cases, dilatancy may be detected earlier, or in the case of porous rocks, only very near the fracture stress [*Brace*, 1978; *Paterson and Wong*, 2005]. The Coulomb yielding criterion, describing the onset of dilatancy, is similar to Coulomb failure criterion and can be written as

$$CYS = \frac{\sigma_1 - \sigma_3}{2} + \sin\varphi_y\left(\frac{\sigma_1 + \sigma_3}{2} + p_f\right) + C_y\cos\varphi_y. \quad (3)$$

Here CYS is the Coulomb Yielding Stress, φ_y and C_y are the friction angle and the cohesion during dilatancy. Parameters φ_y and C_y can be determined in standard laboratory multistage

---

[1]European Technical Centre, M-I SWACO (a Schlumberger Co.), Stavanger, Norway.

triaxial tests [*Fjær et al.*, 2002]. In contrast to *CFS*, the *CYS* can be greater than zero, because for $CYS \geq 0$, the material does not lose rigidity and only microfractures propagate during yielding (thus producing the observed acoustic emissions). Additionally, the parameter C_y in equation (3) is sensitive to the loading/unloading history of rock. For example, if during loading $CYS = A > 0$, then during unloading the deformation should be elastic because no additional microfractures are created and acoustic emissions are suppressed. This is known as the Kaiser effect [*Kaiser*, 1959]. If the sample is reloaded, then no additional microfractures (or acoustic emissions) will develop until overcoming the previous load maximum, for example, $CYS \geq A$. Instead of writing $CYS \geq A$ as the Yield criterion for reloading of the sample, equation (3) can be rewritten for a new cohesion C_y^{new} as

$$CYS = \frac{\sigma_1 - \sigma_3}{2} + \sin \varphi_y \left(\frac{\sigma_1 + \sigma_3}{2} + p_f \right) + C_y^{new} \cos \varphi_y, \quad (4)$$

with $C_y^{new} = C_y^{old} - \frac{A}{\cos \varphi_y}$.

[4] In this way, the onset of marked acoustic emission is controlled by Coulomb Yielding Stress and not by Coulomb Failure Stress. Using *CYS* instead of *CFS* (as a criterion for triggering acoustic emissions) allows an explanation for the Kaiser effect. The acoustic emission analogy during the yielding of rocks is assumed to be the main reason for microseismicity triggering around borehole. Typical values of ΔCFS in the order of 0.01–0.3 MPa appear to be sufficient to trigger seismicity, but are small compared to the magnitudes of tectonic stresses [*King et al.*, 1994; *Stein*, 1999; *Freed*, 2005]. *Kilb et al.* [2002] have demonstrated that the lower bound of ΔCFS leading to increased seismicity rate is surprisingly small, in the order of 0.0005 MPa. Using the *CFS* as a seismicity-triggering mechanism makes it difficult to understand why such a small change of *CFS* is sufficient to trigger the seismicity. *Zoback and Harjes* [1997] suggested that small *CFS* changes trigger seismicity because many faults are critically stressed at depth ($CFS = 0$). However, from the discussion above that this condition is too strong since seismicity can already be triggered from yielding at much lower levels of differential stress. Therefore the Coulomb Yielding Stress (equation (3)) is used here as a seismicity-triggering mechanism. According to this criterion the seismicity is triggered when $CYS \geq 0$ and suppressed when $CYS < 0$. Typically, absolute values of in situ stresses and cohesion are unknown; however, the change of total stresses and pore pressure can be estimated in analogy with equation (2) as follows:

$$\Delta CYS = \Delta \tau + (\Delta \sigma_m + \Delta p_f) \sin \varphi_y. \quad (5)$$

If the state of in situ stresses is away from the yielding point ($CYS < 0$), then the necessary *CYS* change required for seismicity triggering, can be calculated as $CYS + \Delta CYS \geq 0$ (or equivalently $\Delta CYS \geq -CYS$). If in situ stresses are already at the yield surface, then it is sufficient to have $\Delta CYS \geq 0$ for seismicity triggering. If $\Delta CYS < 0$, the seismicity will be suppressed owing to Kaiser effect.

[5] Fluids exert significant mechanical forces that influence microseismicity and earthquake triggering [*Hickman et al.*, 1995]. The role of fluid pressure on strength can be expressed via Terzaghi's effective stress law: $\sigma'_{ij} = \sigma_{ij} + \delta_{ij} p_f$, here σ_{ij} is the stress tensor, negative in compression; and δ_{ij} is the Kronecker delta. Thus, according to equation (3), pore fluid pressure increase will promote earthquake triggering, while a decrease in pore fluid pressure will suppress seismic activity. Importantly, observations show that seismicity can be triggered also during pore pressure reduction in a reservoir [e.g., *Hillis*, 2000], in contradiction to equation (3). This can be understood and explained by considering poroelastic properties. That is, poroelastic contraction of a reservoir reduces the total horizontal stress by $\Delta \sigma_h = 2\eta \Delta p_f$ while the total vertical stress remains constant. This condition takes place for a reservoir with aspect ratio = length/width ≥ 20 [*Segall and Fitzgerald*, 1998]. Here $\eta = \frac{\alpha}{2} \frac{1-2\nu}{1-\nu}$ is the poroelastic stress coefficient [*Economides and Nolte*, 2000], α is the Biot's poroelastic constant, ν is the Poisson's ratio and Δp_f is the pressure change in the reservoir. To explain the oil-production-induced microseismicity, *Rutledge et al.* [1998] modeled the poroelastic contraction of an elliptical reservoir, and demonstrated that the total change of stress in a reservoir driven by oil production is in the order of 0.02 MPa. Oil-production-induced seismicity has also been reported by *Dyer et al.* [1999] and *Kristiansen at al.* [2000]. *Miller et al.* [2004] discussed how the aftershock sequence following by an earthquake in 1997 in Northern Italy was triggered by degassing of a trapped high-pressure source of Carbon Dioxide (CO_2) along a fault zone created during the earthquake and breaching and impermeable seal that confined the high-pressure (70 MPa) CO_2 source below. The aftershock triggering was argued to result from (positive) fluid pressure diffusion above the source, but offered no explanation for the observed seismicity within the source of reduced fluid pressure. In this paper, I argue that fluid pressure reduction also triggers seismicity through seepage forces established in response to fluid pressure gradients.

[6] It has also been reported that pore pressure perturbation fronts trigger seismicity [*Zoback and Harjes*, 1997; *Parotidis et al.*, 2003; *Antonioli et al.*, 2005; *Shapiro et al.*, 2006]. It was recently demonstrated by *Shapiro and Dinske* [2009a, 2009b] that the spatiotemporal distribution of seismic events that scale with the cubic root of time can be explained by mechanisms involving a highly nonlinear fluid diffusion. The nonlinearity of diffusion equation follows from the assumption that the seismicity is triggered by propagation of fluid pressure perturbation front. I argue that this assumption is not correct, because the seismicity should be triggered by the propagation of an effective stress perturbation front, that is, the combination of both the total stress and pore pressure perturbations. Since fluid diffusion changes the magnitudes of total stresses around a borehole owing to poroelastic coupling, these poroelastic effects must be considered. Using the same experimental data as that used to compare to the highly nonlinear fluid diffusion model, I show that the data can be explained simply by coupling of linear diffusion and deformation of a linear poroelastic medium. Models that show seismicity correlations with the propagation of fluid pressure pulse ($\frac{\Delta p_f}{\Delta t}$) using a nonlinear pressure-dependent permeability [see *Miller et al.*, 2004, Figure 3] can also be

explained by a linear diffusion process in a linear poroelastic medium.

2. Theoretical Model

[7] I calculate the change of *CYS* caused by seepage forces and by fluid diffusion, where the seepage forces are forces driven by the gradients of pore fluid pressure [*Mourgues and Cobbold*, 2003; *Rozhko et al.*, 2007]. From the force balance equation for Terzaghi's effective stress, $\sum_j \frac{\partial \sigma'_{ij}}{\partial x_j} = -\rho_t g_i - \frac{\partial p_f}{\partial x_i}$, it is clear that the seepage forces are body forces, like gravitation ($\rho_t g_i$), and act along gradients of fluid pressure, or similarly, along the fluid flow direction. In the equation, ρ_t is the total density and g_i is the component of gravitational acceleration along the x_i coordinate. By analogy between seepage forces and forces of gravitational acceleration, the location of maximum stress changes driven by pore pressure gradients may not coincide with location of the maximum pore pressure gradient. For example, the maximum gravitational acceleration is on the Earth's surface, while maximum compressive stress is in the center of the earth where the gravitational acceleration is zero.

[8] Here I present the analytical solution for the perturbations of stresses and pore fluid pressure caused by the injection/extraction of fluid in/from a borehole. For simplicity, it is assumed that the fluid filtration in a fluid-saturated medium is controlled by a linear diffusion equation derived from fluid-mass conservation and Darcy's law [*Barenblatt et al.*, 1990]:

$$\frac{\partial p_f}{\partial t} = D\vec{\nabla}^2 p_f, \qquad (6)$$

where D is pressure diffusivity constant, $\vec{\nabla}^2$ is Laplace operator, and t is time.

[9] The pressure diffusivity constant is $D = \frac{k_0}{\mu m_0 (\beta_m + \beta_f)}$, where k_0 = permeability (assumed to be an effective stress independent scalar), μ = fluid viscosity, m_0 = porosity, β_m = pore (crack) volume compressibility and β_f = fluid compressibility. Typical values of pressure diffusivity constant for the Earth's crust are between $0.36 - 3.6 \cdot 10^4 \ m^2/h$ [*Parotidis et al.*, 2004]. *Steacy et al.* [2005] have indicated that the pressure diffusivity constant could be order of magnitude higher for geothermal and tectonic areas, that is, up to $3.6 \cdot 10^5 \ m^2/h$.

[10] As discussed below, I assume that the extraction or injection domain of a borehole (associated with perforated or open hole interval) can be approximated by a superposition of spherical cavities along the borehole. Considering a spherical cavity of radius a and at time $t = 0$, an instant step-type fluid pressure perturbation on the cavity wall p_c is imposed. I consider that a fluid pressure perturbation represents the difference between the current fluid pressure and the preexisting reservoir fluid pressure (hydrostatic, for instance). The solution of the three-dimensional diffusion equation (equation (6)) that satisfies the boundary and initial conditions is [*Carslaw and Jaeger*, 1959] $p_f = p_c \frac{a}{r}\left(1 - \text{erf}\left(\frac{r-a}{\sqrt{4Dt}}\right)\right)$, where erf is the error function. Taking into account the distribution of pore pressure pertur-

bation at distances $r \gg a$, the analytical solution can be rewritten in the following form:

$$p_f = p_c \frac{a}{r} f_F(R), \quad f_F(R) = 1 - \text{erf}(R), \qquad (7)$$

where R is the nondimensional variable $R = \frac{r}{\sqrt{4Dt}}$ and $f_F(R)$ is a nondimensional function introduced for simplicity of the analysis below.

[11] The general solution for poroelastic stresses (comprising seepage forces) caused by a spherical fluid source can be calculated by analogy with thermoelasticity as follows [*Timoshenko and Goodier*, 1982; *Rozhko*, 2008]: $\sigma_{rr} = -\frac{4\eta}{r^3}\int_a^r p_f r^2 \, dr + C_1 \frac{C_2}{r^3}$ and $\sigma_{\theta\theta} = \frac{2\eta}{r^3}\int_a^r p_f r^2 dr + C_1 + \frac{C_2}{2r^3} - 2\eta p_f$. Here η is the poroelastic stress coefficient, defined previously; constants C_1 and C_2 are found from the boundary conditions for perturbations of stresses: $\sigma_{rr} = 0$ at $r \to \infty$ and $\sigma_{rr} = -p_c$ at $r = a$. Because of the spherical symmetry, there are only two nonzero stress components in the spherical coordinate system, the radial σ_{rr} and circumferential $\sigma_{\theta\theta}$ stress, which are computed at a distance r from the fluid source. After integration of $\int_a^r p_f r^2 dr$, implementing boundary conditions, and neglecting small terms of order $a/r \ll 1$, the following expressions for the mean and differential stresses are derived:

$$\frac{\sigma_{\theta\theta} + \sigma_{rr}}{2} = \eta p_c \frac{a}{r} f_M(R), \qquad (8)$$

$$\frac{\sigma_{\theta\theta} - \sigma_{rr}}{2} = \eta p_c \frac{a}{r} f_D(R). \qquad (9)$$

Here $f_M(R)$ and $f_D(R)$ are the functions of the nondimensional variable $R = \frac{r}{\sqrt{4Dt}}$, which are calculated as follows:

$$f_M(R) = \frac{1}{2}\left(\text{erf}(R)\left(3 - \frac{1}{2R^2}\right) - 3 + \frac{1}{\sqrt{\pi}}\frac{\exp(-R^2)}{R}\right), \qquad (10)$$

$$f_D(R) = \frac{1}{2}\left(\text{erf}(R)\left(\frac{3}{2R^2} - 1\right) + 1 - \frac{3}{\sqrt{\pi}}\frac{\exp(-R^2)}{R}\right). \qquad (11)$$

[12] Equations (8)–(11) present the solution for stress changes caused by diffusion of a pore fluid pressure perturbation (equation (7)) from a spherical source. This solution is simplified and applicable at distances $r \gg a$. The exact solution is not presented here because it is too cumbersome, and the practical application will be considered only at distances $r \gg a$. This solution is derived for the spherical fluid source, however, in the case of a borehole with diameter $2a$ and the length of the injection interval $2l$, the change of stresses at distance $r > l$ is assumed to be approximately equivalent to the change of stresses driven by l/a spherical fluid sources. Here, the length of the injection interval can be approximated by the length of the perforated interval of a borehole (or the length of an open hole). Thus, in order to apply equations (7)–(11) for the borehole case, one should replace the diameter of the spherical cavity ($2a$) by the length of the injection interval ($2l$); that is, change a to l in equations (7)–(9). After changing a to l, these
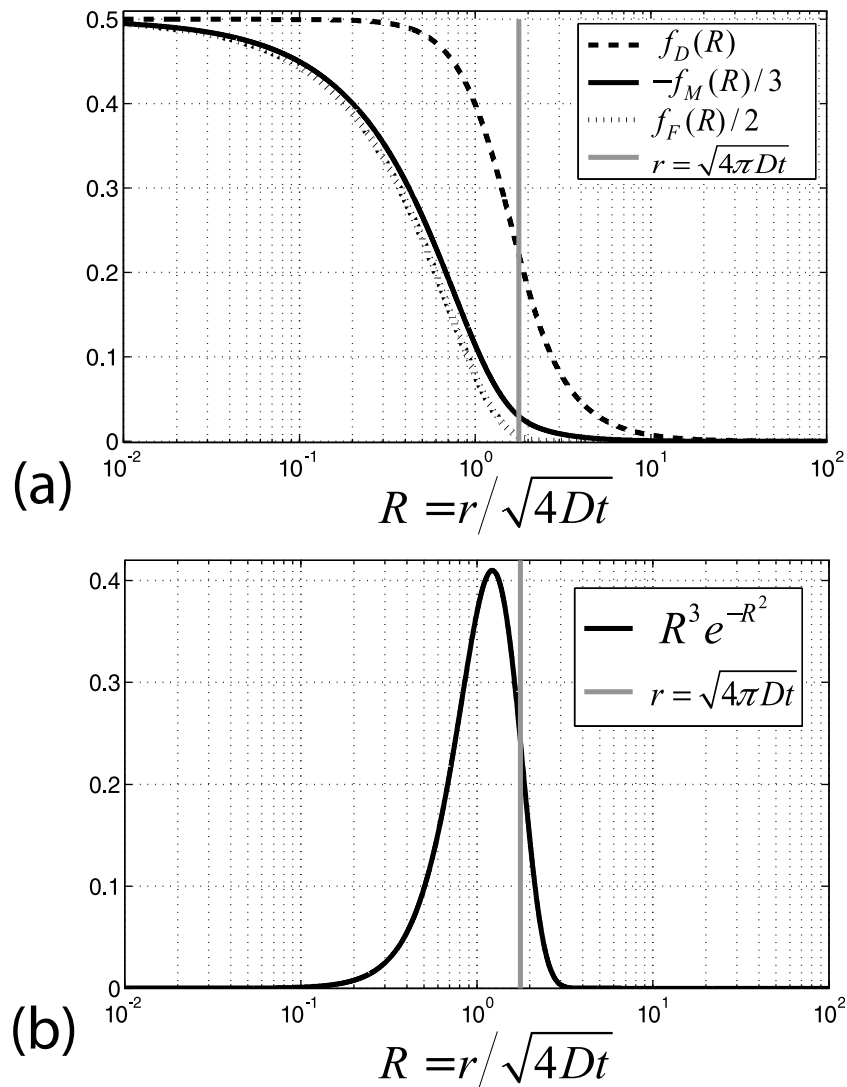
Figure 1. (a) Nondimensional functions responsible for scaling of differential stress (f_D), mean stress (f_M), and fluid pressure (f_F). These functions show that the pressure and mean stress perturbations are negligible on the diffusion front (vertical gray line), while perturbation of differential stress is not negligible. (b) Nondimensional function showing the localization of the fluid pressure pulse close to the diffusion front (vertical gray line).

equations will give the approximate solution for distances $r > l$ with increasing precision with increasing r/l. Higher precision around a borehole is not necessary because the typical resolution of determined offsets of seismic hypocenters is in the order of 10–100 m, that is, comparable with the typical size of fluid injection/extraction interval, which could be in the order of 1–100 m. Therefore, this solution can be used for distances up to the size of fluid injection/extraction interval, that is, $r \geq l$.

[13] Figure 1a shows the functions of $f_D(R)$, $-f_M(R)/3$, and $f_F(R)/2$, where f_M and f_F are multiplied by $-1/3$ and $1/2$, respectively, for better visualization. Figure 1a shows that the fluid pressure perturbation and mean stress are small or negligible on the diffusion front $r = \sqrt{4\pi Dt}$ (shown by vertical gray line), whereas the differential stress function is not small. This explains why "the seismicity has been triggered by surprisingly weak pore pressure perturbations, i.e.,

as low as 0.001–0.1 MPa" [*Shapiro et al.*, 2006, Conclusion]. The calculations in Figure 1a show that it is not necessary to introduce the highly nonlinear fluid diffusion equation to explain the observed seismicity data. See, for example, Figure 5 of *Shapiro and Dinske* [2009a], which shows a sharp transition in fluid pressure on the diffusion front due to nonlinearity of the filtration equation. Some studies [e.g., *Miller et al.*, 2004] explain the seismicity-triggering front from the point of propagation of a fluid pressure pulse. After taking the time derivative of equation (7) the pressure pulse is calculated as: $\frac{\partial p_f}{\partial t} = \frac{4p_c Dl}{r^3} R^3 e^{-R^2}$, where the term $\frac{1}{r^3}$ is responsible for the geometrical divergence of the pressure pulse in a three-dimensional space, while the term $R^3 e^{-R^2}$ is responsible for the spatiotemporal localization of the pressure pulse. The plot of function $R^3 e^{-R^2}$ is shown in Figure 1b. The maximum value of $R^3 e^{-R^2}$ is located at the point $R = \sqrt{3/2}$, that is, close to the diffusion front
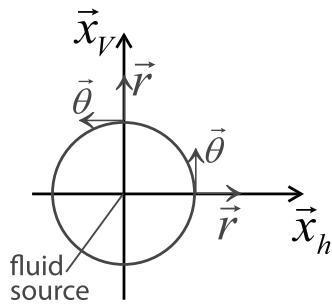
Figure 2. Spherical and Cartesian coordinate systems with the origins at the fluid pressure source. The vertical and horizontal axes coincide with directions of principal maximum and minimum compressive in situ stresses, which are assumed to be along vertical and horizontal directions. During fluid injections the maximum relative increase of *CYS* will be along the direction of minimum in situ stress (left and right) and the maximum relative decrease of *CYS* will be along the direction of maximum in situ stress (top and bottom). The situation is opposite during the fluid extraction (see comments in the text).

(outlined by the vertical gray line) with nonzero stresses in Figure 1a. Using the calculations above (equations (7)–(11)) and Figure 1, it is possible to make an alternative explanation to triggering of increased seismicity rate using the concept of (effective) stress changes instead of propagation of pressure pulses or diffusion fronts.

[14] From equations (8)–(11) it follows that there are only two nonzero stress components driven by seepage forces, σ_{rr} and $\sigma_{\theta\theta}$. These stresses would modify the directions of principal stresses around the borehole. Thus to calculate the change in *CYS* around the fluid pressure source one has to calculate the change in Mohr's circle radius ($\Delta\tau$) and the change of mean stress ($\Delta\sigma_m$). The change of mean total stress is the invariant, that is, does not depend on the coordinate system and can be calculated as follows: $\Delta\sigma_m = \eta p_c \frac{l}{r} f_M(R)$, while the change in Mohr's circle radius depends on mutual orientations of $\vec{x}_V$, $\vec{x}_h$ and $\vec{r}$, $\vec{\theta}$, where $\vec{x}_V$ and $\vec{x}_h$ are coordinate axes along maximum compression in situ stress (vertical) and minimum compression in situ stress (horizontal). $\vec{r}$ and $\vec{\theta}$ are axes in a spherical coordinate system. It is clear that the extreme change in Mohr's circle radius would be localized in space where $\vec{x}_V \parallel \vec{r}$ & $\vec{x}_h \parallel \vec{\theta}$ or where $\vec{x}_V \parallel \vec{\theta}$ & $\vec{x}_h \parallel \vec{r}$, here the symbol "$\parallel$" means that two vectors are parallel. In the case of fluid injection $p_c > 0$, the maximum increase of Mohr's circle radius would be at the location where $\vec{x}_V \parallel \vec{\theta}$ & $\vec{x}_h \parallel \vec{r}$ is equal to $\Delta\tau = \eta p_c \frac{l}{r} f_D(R)$ as shown in Figure 2 (left and right). The maximum decrease of Mohr's circle radius during the fluid injection is the value of $\Delta\tau = -\eta p_c \frac{l}{r} f_D(R)$ at place where $\vec{x}_V \parallel \vec{r}$ & $\vec{x}_h \parallel \vec{\theta}$, as shown in Figure 2 (top and bottom). During production or fluid extraction $p_c < 0$ and the maximum increase of Mohr's circle radius would be at the location where $\vec{x}_V \parallel \vec{r}$ & $\vec{x}_h \parallel \vec{\theta}$ and equals to $\Delta\tau = \eta p_c \frac{l}{r} f_D(R)$, as shown in Figure 2 (top and bottom). The maximum decrease of Mohr's circle radius during the fluid extraction is located where $\vec{x}_V \parallel \vec{\theta}$ & $\vec{x}_h \parallel \vec{r}$ and equals $\Delta\tau = \eta p_c \frac{l}{r} f_D(R)$ (see Figure 2, left and right). The change in *CYS* during fluid injections and extractions can be calculated on the basis of the discussions above as follows:

$$\Delta CYS_{\max} = \eta |p_c| \frac{l}{r} f_D(R) + p_c \frac{l}{r} (\eta f_M(R) + f_F(R)) \sin\varphi_y, \quad (12)$$

$$\Delta CYS_{\min} = -\eta |p_c| \frac{l}{r} f_D(R) + p_c \frac{l}{r} (\eta f_M(R) + f_F(R)) \sin\varphi_y, \quad (13)$$

where $\Delta CYS_{\max}$ and $\Delta CYS_{\min}$ are the maximum and minimum values of *CYS* change.

[15] It is important to note here that it has been predicted that if σ_V is the maximum compressive in situ stress along the vertical direction, then the induced seismicity data caused by fluid injection would be observed at the same depth as the fluid-injection interval and localized along the direction of minimum compressive in situ stress σ_h. Experimental data shows that the microseismicity induced by hydraulic fracturing operations in Barnett shale is located at the same depth as the fluid-injection source [see *Shapiro and Dinske*, 2009b, Figure 3] and is elongated along a certain direction [see *Shapiro and Dinske*, 2009b, Figure 4]. In the case of fluid extraction from a borehole (production) it is shown that the seismicity would be localized above and below the fluid extraction (perforation) interval because that is the maximum increase in *CYS*. Field observations reported by *Rutledge et al.* [1998] demonstrated that seismicity has been triggered both above and below the drained interval, while observations reported by *Kristiansen et al.* [2000] showed that the observed seismicity occurred only above the drained interval. The reason why no seismicity was observed below the production interval can be explained by the differences of in situ stresses below and above. That is, the change of *CYS* required to trigger seismicity was lower on the top. Additionally, the difference in rock strength below and above the drained interval might also contribute to this observation. The direction of maximum in situ compressive stress is typically vertical (in extension environments), and may be the reason why the aforementioned location of earthquakes hypocenters correlates well with the theoretical predictions. However, if the directions of principal stresses do not coincide with vertical and horizontal axes, then the location of the observed seismicity data can be explained by analogy with the discussions above.

3. Scaling of Fluid-Induced Seismicity

[16] Figure 3 shows the induced seismicity data during borehole fluid injection into the Barnett shale. The data are taken from *Shapiro and Dinske* [2009a]. The borehole pressure (measured in the injection domain) and fluid flow rate are shown in Figure 3 (top). Offsets of microearthquakes' hypocenters from the fluid-injection domain as a function of time are shown in Figure 3 (middle and bottom) with black curves representing seismicity-triggering fronts predicted for square and cube root of time scalings. The black curve in Figure 3 (bottom) (representing the seismicity-triggering front) is the solution of equation (12) with the following parameters: $\Delta CYS_{\max} = 0.3$MPa (assumed value, which depends on in situ stresses and rock strength, as discussed in
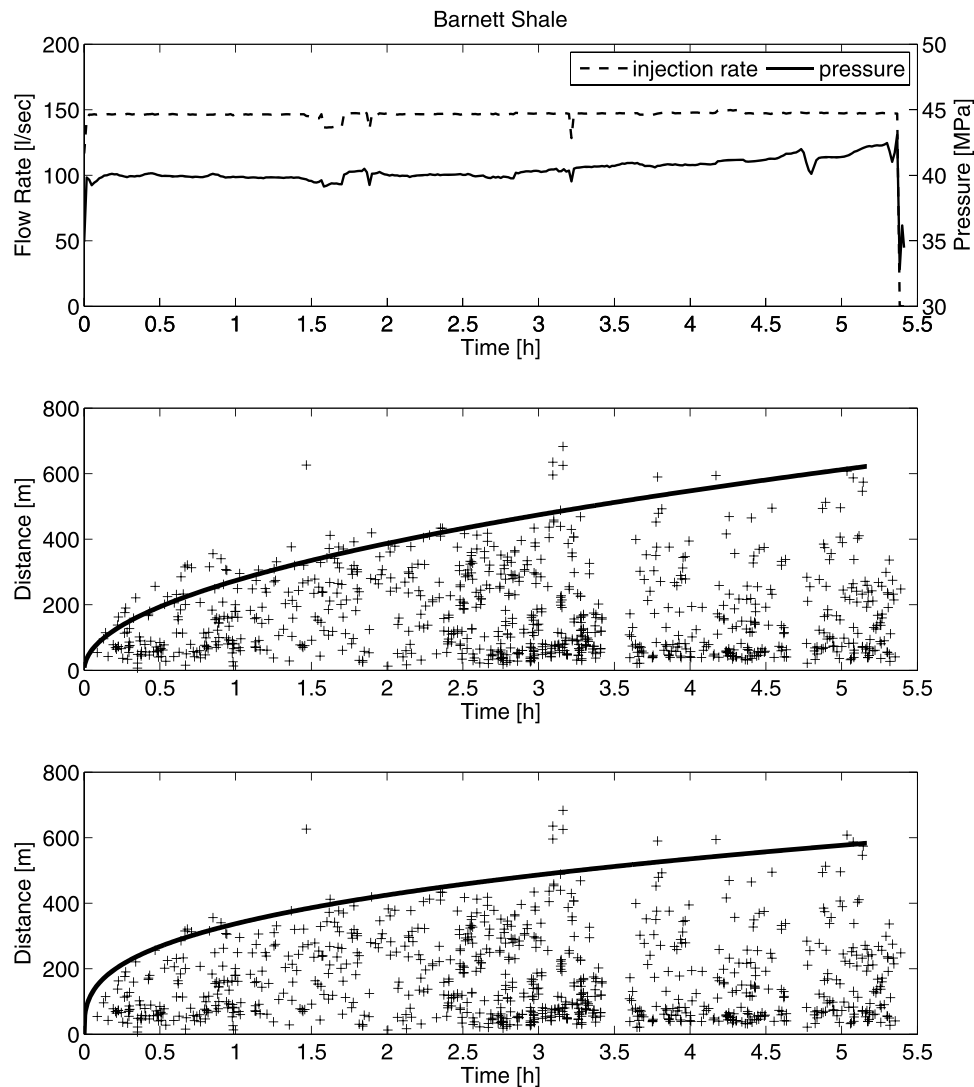
Figure 3. Seismicity induced by borehole fluid injection in Barnett Shale (data are taken from *Shapiro and Dinske* [2009a]). (top) Borehole pressure (measured at the injection domain) and fluid flow rate. (middle and bottom) The time-distance plots of induced microseismic events, where the distance is measured from the center of fluid-injection interval. The black curve in the middle plot shows scaling of seismicity front as a square root of time, while the black curve in the bottom plot shows scaling of seismicity front as a cubic root of time. The black curve shown in the bottom plot is predicted using equation (12) with f_F, f_M, and f_D defined in equations (7), (10), and (11), described in the text.

introduction), p_c = 40 MPa (known), η = 0.25 (assumed, typical for reservoir rock), $2l$ = 100 m (assumed length of injection interval), φ_y = 30° (assumed value for reservoir rock) and D = 9500 m^2 (is determined from fitting of induced seismicity data). Note here that D = 9500 m^2/h is the "apparent" value of hydraulic conductivity, which is much higher than the typical value of an (almost impermeable) unfractured shale. This high value (D = 9500 m^2/h) corresponds to diffusivity in fractured shales, where the increased permeability is caused by hydraulic fracturing operation. I use the term "apparent" value of hydraulic conductivity because it is indirectly determined from analysis of passive seismic data, and depends on assumed values of Biot's constant, Poisson's ratio and the angle of internal friction. Better the constraints on these parameters reduces

the uncertainty in hydraulic conductivity. Hydraulic fracturing during injection increases the hydraulic conductivity, so laboratory derived values of D are of little value. The value of D (and thus permeability) can be estimated from interpretation of spatiotemporal distribution of microseismicity. As recently demonstrated by *Shapiro and Dinske* [2009a], scaling as the cubic root of time fits the experimental data better than the square root of time as predicted by the propagation of fluid diffusion front. Figure 4 shows different seismicity-triggering fronts, predicted using equation (12) and plotted versus the cubic root of time. Intrinsic properties of the reservoir (η, φ_y, & D) are kept constant, while different injection conditions (p_c & l) are imposed. According to equation (12), the different shapes of seismicity-triggering fronts $\Pi_1 - \Pi_6$ (Figure 4) are controlled by the following
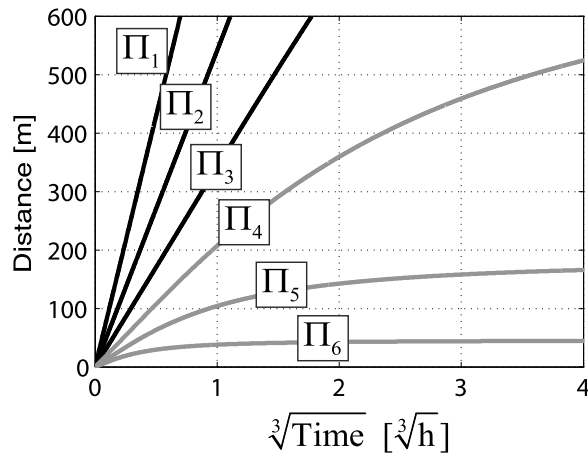
Figure 4. Seismicity-triggering fronts (predicted using equations (12), (7), (10), and (11)) as a function of cubic root of time. The line Π_3 corresponds to the black curve in Figure 3 (bottom), thus it proves the cubic root behavior. Curves $\Pi_1 - \Pi_6$ are generated using different injection conditions (p_c & l), as described in the text, while intrinsic properties (η, φ_y & D) were fixed. Curves $\Pi_1 - \Pi_3$ are scaled as a cubic root of time, while curve Π_6 shows no time dependence for time >1 h and curves Π_4 and Π_5 reveal the intermediate situation.

combination of parameters: $\Pi = l p_c / \Delta CYS_{\max}$, provided that η, φ_y, & D are fixed. Thus, for curve Π_3 this parameter is equal to $\Pi_3 = \frac{50m \cdot 40MPa}{0.3MPa} \simeq 6.7$ km and for other curves the following relations are imposed: $\Pi_1 = 16\,\Pi_3$, $\Pi_2 = 4\,\Pi_3$, $\Pi_4 = \Pi_3 / 4$, $\Pi_5 = \Pi_3 / 16$ and $\Pi_6 = \Pi_3 / 64$. The shape of curves $\Pi_1 - \Pi_3$ are consistent with a cubic root of time scaling, while the dependence on time for curves $\Pi_4 - \Pi_6$ is much weaker. If $\Pi < \Pi_6$ there would be almost no dependence on time and if $\Pi > \Pi_3$, all seismicity-triggering fronts are scaled as a cubic root of time. If the increased *CYS* does not change in time (curve Π_6 in Figure 4), the induced seismicity rate should be suppressed after certain period of time owing to viscoelastoplastic relaxation of stresses, but this effect is not considered here.

[17] These calculations are applicable for the constant fluid pressure source; however, if the borehole fluid pressure increases with time it will affect the scaling of the seismicity-triggering front. Using the principle of linear superposition of stresses it is possible to modify the theoretical model (equation (12)) to predict the induced seismicity front for the known time dependence of the borehole fluid pressure.

4. Reservoir Characterization by the Analysis of the Seismicity-Triggering and Seismicity-Suppression Fronts

[18] Figure 5 shows induced seismicity related to a "hydraulic fracturing operation" in Barnett shale [*Shapiro and Dinske*, 2009b]. The borehole pressure (measured at the injection domain) and fluid flow rate are shown in Figure 5 (top), while Figure 5 (bottom) shows the spatio-temporal distribution of induced seismicity data; the black curve shows the predicted seismicity-triggering front, while the gray curve shows the predicted seismicity-suppression

front (or back front), caused by termination of fluid injection in a borehole. Here I show how to apply the above theory to predict seismicity-triggering and -suppression fronts. It will also be demonstrated how the seismicity-triggering and -suppression fronts can be applied for reservoir modeling and characterization.

[19] Figure 5 (top) shows that at time $t_0 = 0$ the borehole (bottomhole) fluid pressure has increased to 40 MPa and remains constant until $t_1 = 5.4$ h. Small oscillations in bottomhole pressure are neglected here for simplicity. For the time $t > t_1$ the bottomhole pressure has decreased rapidly to its in situ value. The in situ value of pore fluid pressure was assumed to be about 30 MPa, equal to the bottomhole pressure at zero injection rate before and after fluid injection. Thus the pressure perturbation during hydraulic fracturing operation was about 10 MPa. To calculate the change in *CYS*, the fluid pressure perturbation source at a borehole can be represented as; $p_c = H(t - t_0)p_{c0} + H(t - t_1)p_{c1}$ where the $H(t)$ is the Heaviside step function defined as $H(t) = \begin{cases} 0 & \text{if} \quad t < 0 \\ 1 & \text{if} \quad t > 0 \end{cases}$, and where $p_{c0} = 10$ MPa and $p_{c1} = -10$ MPa. Such choices of p_{c0} and p_{c1} approximate the bottomhole fluid pressure as shown in Figure 5. To predict the shapes of seismicity-triggering and -suppression fronts it has been assumed that the "apparent" value of pressure diffusivity constant for positive fluid pressure per-
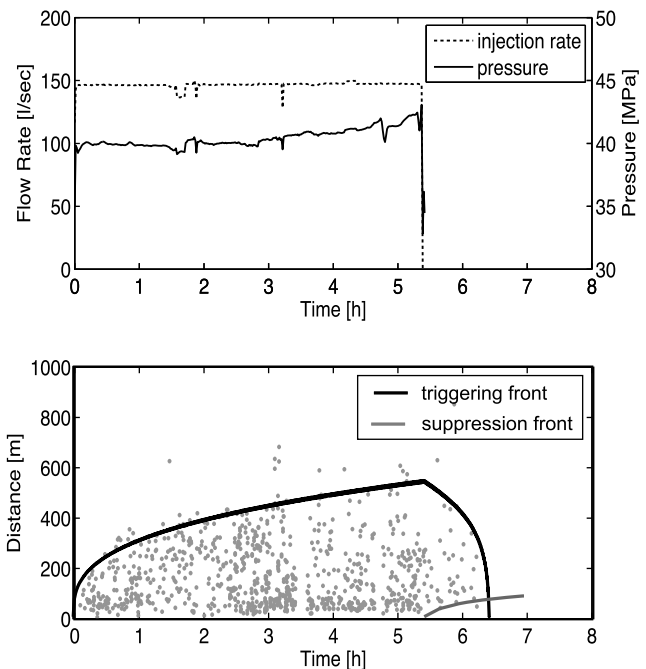

Figure 5. Seismicity induced by fluid injection in Barnett Shale (data from *Shapiro and Dinske* [2009b]). (top) Borehole pressure (measured in injection domain) and fluid flow rate as a function of time. (bottom) Spatiotemporal distribution of induced seismic events. Black curve is seismicity-triggering front, predicted with equation (14). Gray curve is seismicity-suppression front, caused by termination of fluid injection into a borehole, predicted with equations (16) and (17).

turbation (p_{c0}) is different from "apparent" pressure diffusivity constant for negative fluid pressure perturbation, that is, $D_0 \neq D_1$. This difference is introduced for two reasons: (1) it was not possible to explain the seismicity-triggering and -suppression fronts using the same values of D, and (2) the value of D_0 corresponds to fluid diffusion during the process of hydraulic fracturing, while the value of D_1 corresponds to diffusion of negative fluid pressure perturbation in already fractured rocks. For that reason, D_1 should be higher than D_0. Please note here that the difference between D_0 & D_1 does not imply the pressure-dependent permeability. It implies only the difference in permeability before and after fluid injection. Using superposition of stresses during positive and negative hydraulic loadings and equations (12) and (13), I calculated the changes of CYS along the horizontal direction of minimum compressive in situ stress ΔCYS_h and along the vertical direction of maximum compressive in situ stress ΔCYS_V as follows:

$$\Delta CYS_h = \frac{l}{r}p_{c0}\mathrm{H}(t - t_0)\Big[\eta f_D(R_0) + (\eta f_M(R_0) + f_F(R_0))\sin\varphi_y\Big] + \cdots$$
$$\cdots + \frac{l}{r}p_{c1}\mathrm{H}(t - t_1)\Big[\eta f_D(R_1) + (\eta f_M(R_1) + f_F(R_1))\sin\varphi_y\Big]$$
(14)

$$\Delta CYS_V = \frac{l}{r}p_{c0}\mathrm{H}(t - t_0)\Big[-\eta f_D(R_0) + (\eta f_M(R_0) + f_F(R_0))\sin\varphi_y\Big] + \cdots$$
$$\cdots + \frac{l}{r}p_{c1}\mathrm{H}(t - t_1)\Big[-\eta f_D(R_1) + (\eta f_M(R_1) + f_F(R_1))\sin\varphi_y\Big],$$
(15)

where $R_0 = r/\sqrt{4D_0(t - t_0)}$ and $R_1 = r/\sqrt{4D_1(t - t_1)}$. From equations (14) and (15) one can see that the CYS change in the horizontal direction is always higher than in the vertical direction, that is, $\Delta CYS_h > \Delta CYS_V$. Therefore, equation (14) has been used to predict the shape of the seismicity-triggering front (black curve in Figure 5, bottom).

[20] To calculate the shape of the seismicity-suppression front (gray curve in Figure 5, bottom), it should be taken into account that the fracturing process in the damaged zone below the seismicity-triggering front has locally changed the state of in situ stress. Therefore, the direction of maximum in situ compressive stress locally in the failed zone may not coincide with vertical direction. In addition, it is not correct to apply the principle of superposition of stresses to calculate the CYS change in rocks during fracturing, so that equation (14) is not applicable to predict the shape of seismicity-suppression front. Using the argument that the direction of principal in situ stresses in the failed zone is different from direction of in situ stresses in the far-field zone, the maximum possible change of CYS in the failed zone can be estimated using the poroelastic analytical solution as follows:

$$\Delta CYS_* = \frac{l}{r}p_{c0}\mathrm{H}(t - t_0)\Big[\eta f_D(R_0) + (\eta f_M(R_0) + f_F(R_0))\sin\varphi_y\Big] + \cdots$$
$$\cdots + \frac{l}{r}p_{c1}\mathrm{H}(t - t_1)\Big[-\eta f_D(R_1) + (\eta f_M(R_1) + f_F(R_1))\sin\varphi_y\Big].$$
(16)

Note that $\Delta CYS_* > \Delta CYS_h$. To calculate the shape of seismicity-suppression front, the following equation has been

solved, comprising the Kaiser effect (i.e., the onset where the maximum value of CYS starts to decrease), which can be formulated as follows:

$$\Delta CYS_* - \sup\{\Delta CYS_h : t > 0\} = 0.$$
(17)

Here $\sup\{\Delta CYS_h : t > 0\}$ is the maximum or least upper bound of CYS along the direction of (σ_h). The function $\sup\{\Delta CYS_h : t > 0\}$ depends on the distance (r) from the fluid-injection source and is equivalent to parameter (A) explained in section 1 (see equation (3)). Now using equations (14), (16), and (17), the shapes of seismicity-triggering and seismicity-suppression fronts can be predicted (Figure 5, black and gray curves). The following input parameters were used: $2l = 100$ m (known length of injection interval); $\varphi_y = 30°$ (assumed angle of internal friction at the onset of yielding); $p_{c0} = 10$ MPa and $p_{c1} = 10$ MPa (known pressures for corresponding times $t_0 = 0$ and $t_1 = 5.4$ h), and performing a systematic search of other parameters to find those that give the best fit to experimental data the following parameters have been found: $\Delta CYS_h = 0.025$ MPa; $\eta = 0.3$, $D_0 = 2 \cdot 10^3 \frac{m^2}{h}$ and $D_1 = 2 \cdot 10^3 \frac{m^2}{h}$. Note that the fitting of experimental observations is based only on visual inspection, which is sufficient because the resolution of determined offsets of seismic hypocenters has the order of 10–50 m. Note the very small change of CYS required to trigger the microseismicity (compared to the magnitudes of in situ stresses at depth more than 2 km). This is be explained by in situ stresses that are beyond the elastic limit and near the yield state.

[21] It is interesting to note that the fluid injection took place during the time $t_1 - t_0 = 5.4$ h. During that period the size of diffusion front (for positive perturbation of fluid pressure p_{c0}) is calculated as $r_{d0} = \sqrt{4\pi D_0(t_1 - t_0)} \approx 368$ m, while the size of triggering front at time = 5.4 h according to Figure 5 is ≈ 550 m. Thus the seismicity-triggering front during fluid injection propagates faster than the fluid diffusion front. This can be explained by the calculations shown in Figure 1a, which shows that the perturbations of differential stress propagates faster than the perturbations of mean stress and faster than the perturbation of fluid pressure. Thus, the seismicity has been triggered by perturbation of differential stress, or equivalently by the increase of Mohr's circle radius.

[22] Another interesting observation is that (see Figure 5) the seismicity has been completely suppressed after time $t_* \geq 6.3$ h. At that time, the size of diffusion front for negative perturbation of fluid pressure (p_{c1}) reached the distance $r_{d1} = \sqrt{4\pi D_1(t_* - t_1)} \approx 368$ m. Surprisingly these two distances are equal, that is, $r_{d0} = r_{d1}$. In other words the seismicity has been completely suppressed when the size of depletion front (after termination of fluid injection) reached the size of injection front (before termination of fluid injection).

[23] One more example to validate the theoretical model is fluid-induced seismicity at Felton Hill, a Hot Dry Rock geothermal energy site in New Mexico in 1983 (Figure 6) (data from *Rothert and Shapiro* [2007]). During massive water injection that lasted approximately 61.1 h at the depth of 3640 m, 11366 microseismic events were recorded with the accuracy less than 100 m using analysis of *P* and *S* seismic waves. Fluid injection took place along an open hole interval
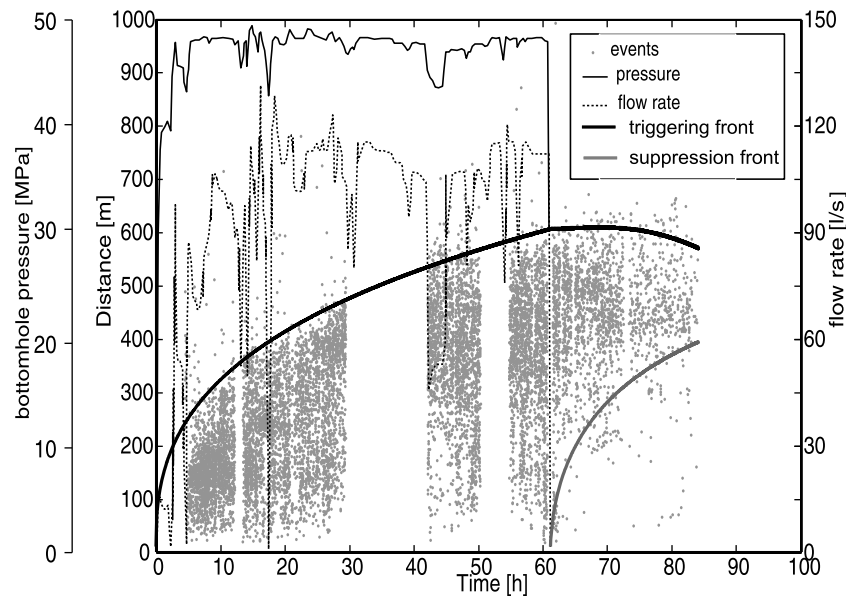
Figure 6. Seismicity induced by fluid injection in Hot Dry Rock at Felton Hill (data are taken from *Rothert and Shapiro* [2007]). Borehole fluid pressure, flow rate, and induced seismicity data are shown on the same plot. White gaps in seismicity (for example, between 30 and 42 h) are due to damage of seismic recording system, and no seismic measurements were performed after 84 h. Black curve is seismicity-triggering front, predicted by equation (14), while gray curve is seismicity-suppression front, predicted by equations (16) and (17).

of approximately 20 m with a nearly constant bottomhole fluid pressure of 48 MPa. The vertical gaps of induced seismicity (as shown in Figure 6) with the largest gap between 30 and 42 h are due to damage of the data recording system and no measurements of induced seismicity recorded after about 84 h. To predict the shape of the seismicity-triggering front (black curve in Figure 6) and seismicity-suppression front (gray curve in Figure 6), the following input parameters have been used: known overpressure [*House*, 1987] of 14 MPa, that is, $p_{c0} = 14$ MPa and $p_{c1} = -14$ MPa with corresponding times $t_0 = 0$ and $t_1 = 61.1$ h. The angle of internal friction at the onset of yielding was assumed to be $\varphi_y = 30°$. The systematic investigation of parameters using equations (14), (16), and (17) reveals that the best fit of seismicity-triggering and seismicity-suppression fronts is obtained using the following values: $\Delta CYS_h = 0.023$ MPa, $\eta = 0.1$, $D_0 = 1.5 \cdot 10^3 \frac{m^2}{h}$ and $D_1 = 2 \cdot 10^3 \frac{m^2}{h}$. The calculations illustrate that the determined change in "apparent" hydraulic diffusivity constants (D_1/D_0) during water injection at Felton Hill site (Figure 6) was much lower than during water injection in Barnett shale (Figure 5) and these two reservoirs have quite different poroelastic stress coefficients, while the state of in situ stresses are close to yielding. Thermoelastic effects (caused by temperature difference between injected fluid and rock, surrounding the wellbore) are not considered here, however it is clear that this effect may have a strong impact on interpretation of parameters of the reservoir.

[24] It is also interesting to estimate the size of fluid pressure perturbation front during water injection to Felton Hill geothermal reservoir. Analogous to the above calculation the size of fluid pressure perturbation front before termination of fluid injection is calculated as follows: $r_{d0} = \sqrt{4\pi D_0(t_1 - t_0)} \approx 1073$ m. However, the size of seismicity-

triggering front at time $t_1 = 61.1$ according to Figure 6 was about 600 m. Therefore in that case, the seismicity has been triggered by increase of Mohr's circle radius and movement of Mohr's circle toward the yielding (or failure) envelope. No seismicity was recorded after 84 h, so it is not possible to say when the seismicity was completely suppressed. However, assuming here (in analogy with Barnett shale) that the seismicity has to be completely suppressed when the size of depletion front (after termination of fluid injection) reached the size of injection front (before termination of fluid injection), in that case the time when the seismicity has to be suppressed can be estimated as follows $t_* = \frac{D_0}{D_1}(t_1 - t_0) + t_1 \approx 107$ h.

[25] In this section, I discussed how the reservoir can be characterized by an analysis of seismicity-triggering and -suppression fronts. This analysis also permits an estimation of the "apparent" hydraulic diffusivity constant (and thus permeability) during passive seismicity monitoring during borehole fluid injection, and estimates of the size of fluid pressure perturbation front. This is important information, particularly during monitoring of waste injection. The theoretical model, described in this chapter can also be expanded to more general time-dependent borehole fluid injection. In section 5, the conditions for induced seismicity during fluid production (extraction) are analyzed.

5. Fluid-Production-Induced Seismicity

[26] Published experimental data demonstrates that oil-production-induced seismicity was observed above a drained depth interval [*Dyer et al.*, 1999; *Kristiansen et al.*, 2000] or both above and below the drained depth intervals [*Rutledge et al.*, 1998]. The reasons why microseismicity was observed there were explained in section 2 of this paper. In this section
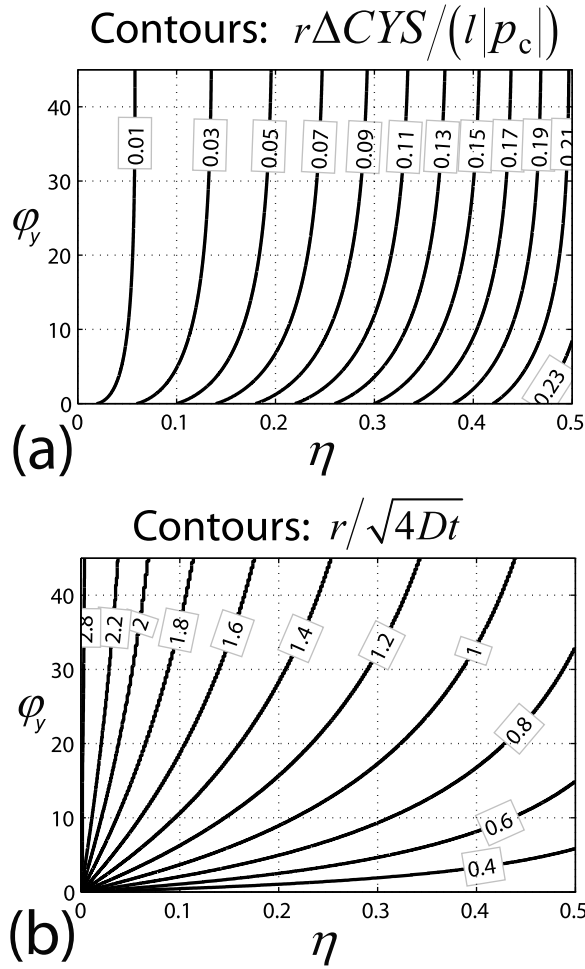
Figure 7. Spatiotemporal distribution of Coulomb Yielding Stress increase during production, calculated using equation (18). (a) Contours show the maximum increase of CYS at distance r from the center of drained interval of length $2l$ with prescribed pressure drop $|p_c|$ as a function of internal friction angle and poroelastic stress coefficient (of rock surrounding a borehole). (b) Contours are inferred to time, when the maximum increase of CYS occurs at distance r.

the maximum change of CYS is calculated, driven by constant drawdown pressure during fluid production starting at zero time. Since the drawdown pressure causes a negative fluid pressure perturbation in a reservoir, then equation (12) can be rewritten as follows:

$$\frac{\Delta CYS}{|p_c|}\frac{r}{l} = \eta f_D(R) - (\eta f_M(R) + f_F(R))\sin\varphi. \quad (18)$$

Figures 7a and 7b show a numerical solution of equation (18), where Figure 7a depicts the maximum value of $\frac{\Delta CYS}{|p_c|}\frac{r}{l}$ as a function of η and φ_y and Figure 7b shows the spatiotemporal location $R = \frac{r}{\sqrt{4Dt}}$ of the maximum value of $\frac{\Delta CYS}{|p_c|}\frac{r}{l}$ as a function of η and φ_y. For example, if the friction angle of rock surrounding a wellbore is $\varphi_y = 30°$ and the poroelastic stress coefficient is $\eta = 0.3$, then from Figures 7a and 7b one can see that $\frac{\Delta CYS}{|p_c|}\frac{r}{l} \approx 0.1$ and $\frac{r}{\sqrt{4Dt}} \approx 1.2$. Therefore, the maximum change of CYS at distance r from the fluid draw-

down pressure source $|p_c|$ of length $2l$ would be $\Delta CYS \approx 0.1\frac{l}{r}|p_c|$ at time $t \approx \frac{r^2}{4D(1.2)^2}$. If time $t > \frac{r^2}{4D(1.2)^2}$ the change of CYS will decrease and thus the microseismicity will be suppressed at the offset r. It is also interesting to note that according to Figure 7a, the highest increase in CYS would be in rocks with low angles of internal friction and high values of poroelastic stress coefficient η, which depends on Biot's constant (α) and on Poisson's ratio (ν) as follows: $\eta = \frac{\alpha}{2}\frac{1-2\nu}{1-\nu}$. The typical value of Biot's constant for sandstones and highly porous chalk is close to 1, while the typical values of Poisson's ratio for chalk and sandstones are around 0.2–0.35. The typical values of friction angle for sandstones and chalks are around 20°–35°. Hence the maximum increase of CYS for chalks and sandstones at distance $r \approx l$ according to Figure 7a would be around $\Delta CYS \approx 0.15|p_c|$, and according to Figure 7b this would take place at time $t \approx \frac{l^2}{4D}$. Consequently, if the depletion pressure ($|p_c|$) is sufficiently high, the failure above or below the drained interval may lead to an instability of a borehole and sand/chalk production [*Fjær et al.*, 2002] from the failed area above or below the drained interval. To reduce the risk of wellbore instability and sand/chalk production, it is recommended in accordance with calculations above to increase slowly (in comparison with time $t = \frac{l^2}{4D}$) the drawdown pressure ($|p_c|$) at a borehole. For instance, if the anticipated drawdown pressure is p_*, then the maximum pressure increase rate during initiation of production should be $\frac{4D}{l^2}p_*$.

[27] The calculations above are developed for infinite reservoirs. However, real reservoirs have a finite width. If h is the distance between the perforation interval and impermeable seal caprock, then the calculations above are applicable when the size of depletion front is smaller than h, that is, $\sqrt{4\pi Dt} \leq h$.

6. Discussion

[28] Pressure-dependent permeability is a well-known phenomenon that introduces a nonlinearity to the fluid filtration equation. This nonlinearity was recently reported to be responsible for spatiotemporal distribution of fluid-induced seismicity data [*Shapiro and Dinske*, 2009a, 2009b]. This paper demonstrated that linear diffusion in a poroelastic medium can also explain the observed spatiotemporal evolution, so it is not necessary to include nonlinear diffusion. Although this nonlinearity may potentially improve the explanation of field data, its effect is not dominant and should be included with other potentially important effects (but relatively minor for the cases studied in this paper) such as thermoelastic stresses, nonlinear elastoplastic rheology surrounding a borehole, geological structure of a reservoir, anisotropic and heterogeneous permeability, poroelastic constants and strength and multiphase-fluid flow. These effects, however, may play important roles in other cases of fluid-induced seismicity. Thermoelastic effects may be important, but it is difficult to distinguish because of the same diffusive-type nature of thermoelasticity and poroelasticity [*Rozhko*, 2008]. Effects of partial saturation on the strength of shale was not considered in this paper, however it was recently predicted that during desaturation by water injection into tight gas shale reservoir, the strength of shale can significantly decrease up to 10–100 times

owing to changes in capillary forces [*Rozhko*, 2010]; this definitely will promote the microseismicity triggering and has to be studied separately.

[29] The theoretical model proposed in this paper differs from the model described by *Shapiro and Dinske* [2009b] in the following aspects.

[30] 1. According to equation (17) of *Shapiro and Dinske* [2009b], the seismicity-triggering front for the constant fluid pressure source (or equivalently for the source with constant strength) can be scaled with functions bounded by two limits between square and cubic root of time scaling. The experimental data [*Shapiro and Dinske*, 2009a, Figure 1] show that the dependency of the seismicity-triggering front on time is slower than predicted with a cubic root of time scaling, despite slightly increasing fluid-injection pressure. According to calculations presented here (Figure 4), the seismicity-triggering front can be scaled by the cubic root of time or by a time-independent value. Therefore this theoretical model can potentially provide a more satisfactory explanation of the experimental observations.

[31] 2. Using the model presented by *Shapiro and Dinske* [2009b], it is difficult to explain the induced microseismicity caused by fluid extraction from a borehole. However, the model presented here predicts the increase of a Mohr's circle radius during fluid extraction, which may trigger seismicity.

[32] 3. To derive the theoretical model, *Shapiro and Dinske* [2009b] used the assumption that the increased seismicity rate has been triggered by a fluid pressure perturbation front. Using that assumption the authors concluded that the diffusion process must be highly nonlinear in order to explain the cubic root of time scaling. Also in the model of *Miller et al.* [2004], the pressure-dependent permeability was calibrated using scaling arguments of fluid-induced seismicity data. This is not correct because the *CYS* perturbation front and fluid pressure perturbation front are scaled with different scaling laws (see section 3). I demonstrated that the increased microseismicity has been triggered by propagation of an effective stress perturbation caused by fluid diffusion coupled with poroelastic deformation. Depending on in situ conditions, the sufficient change of stresses required to trigger increased microseismicity could be either inside or outside of the diffusion front (or coincide with the diffusion front).

[33] 4. Another advantage of the theoretical model presented here is the possibility to estimate the apparent hydraulic diffusivity constant (and permeability) during and after fluid-injection operation by fitting the shape of seismicity-triggering and -suppression fronts. This type of analysis was not discussed in the model of *Shapiro and Dinske* [2009b].

[34] 5. The model presented here enables the prediction of the shape of seismicity-triggering front after termination of fluid injection into a borehole, which is not well explained by the model of Shapiro and coworkers (compare Figures 5 and 6 in this paper with corresponding Figure 5 of *Shapiro and Dinske* [2009b] and Figure 14 of *Rothert and Shapiro* [2007]).

[35] 6. All intrinsic parameters of rocks used in this model have transparent physical meanings and can be constrained independently by laboratory measurements. Therefore this model can also be used to predict induced microseismicity-triggering fronts on the basis of available intrinsic rock properties, such as Biot's constant, Poisson's ratio, pressure

diffusivity coefficient and angle of internal friction. In contrast, the highly nonlinear power law coefficient used in the pressure-dependent permeability model of *Shapiro and Dinske* [2009b] is deduced from the analyses of a seismicity-triggering front assuming it coincides with the diffusion front, and cannot be corroborated by independent laboratory experiments.

[36] The proposed model does not exclude the importance of nonlinear fluid diffusion. However, as shown here, nonlinear properties should only be considered if all linear properties and processes fail to explain the experimental data. If it is possible to explain the experimental data with linear poroelasticity, then it is not necessary to consider a nonlinear diffusion.

7. Conclusions

[37] In this paper I demonstrated that the measured microseismicity during injection and depletion in reservoirs can be explained by the simple linear poroelasticity equations. The poroelastic stress coefficient is responsible for "nonlinear" coupling of fluid diffusion into elastic stress response. It was also shown that seismicity is triggered by the propagation of a Coulomb Yielding Stress perturbation with time. During fluid injection the seismicity would be localized along the minimum principal in situ compressive stress direction, while during fluid extraction the induced seismicity would be localized along the direction of maximum compressive stress. The change of Coulomb Yielding Stress is explained by seepage forces, as well as the changes in effective stresses. These body forces are caused by the gradients in the pore fluid pressure. The calculations indicate that during fluid injection into a borehole with constant fluid pressure source, the induced seismicity-triggering fronts can be scaled in the range from the cubic root of time to almost time-independent scaling, while the fluid diffusion front requires a square root of time scaling. It was also shown how to apply the shape of back-triggering (suppression) front to estimate the increase in hydraulic diffusivity (and permeability) after termination of fluid injection in a borehole.

[38] Using the same theoretical model it was shown that seismicity can also be induced during production, that is, during depletion of fluid pressure at a borehole. The corresponding spatiotemporal distribution of the Coulomb Yielding Stress is predicted analytically.

References

Antonioli, A., D. Piccinini, L. Chiaraluce, and M. Cocco (2005), Fluid flow and seismicity pattern: Evidence from the 1997 Umbria-Marche (central Italy) seismic sequence, *Geophys. Res. Lett.*, *32*, L10311, doi:10.1029/2004GL022256.

Barenblatt, G. I., V. M. Entov, and V. M. Ryzhik (1990), *Theory of Fluid Flows Through Natural Rocks: Theory and Applications of Transport in Porous Media*, 412 pp., Springer, New York.

Barron, K. (1971), Detection of fracture initiation in rock specimens by the use of a simple ultrasonic listening device, *Int. J. Rock Mech. Min. Sci. Geomech. Abstr.*, *8*, 55–59, doi:10.1016/0148-9062(71)90038-6.

Brace, W. F. (1978), Volume changes during fracture and frictional sliding: A review, *Pure Appl. Geophys.*, *116*, 603–614, doi:10.1007/BF00876527.

Carslaw, H., and J. Jaeger (1959), *Conduction of Heat in Solids*, Oxford Univ. Press, New York.

Dyer, B. C., R. H. Jones, J. F. Cowles, O. Barkved, and P. G. Folstad (1999), Microseismic survey of a North Sea reservoir, *World Oil, March*, 74–78.

Economides, M. J., and K. G. Nolte (2000), *Reservoir Stimulation*, 3rd ed., 856 pp., John Wiley, New York.

Fjær, E., R. M. Holt, A. M. Horsrud, A. M. Raaen, and R. Risnes (2002), *Petroleum Related Rock Mechanics*, 514 pp., Elsevier Sci., New York.

Fortin, J., S. Stanchits, G. Dresen, and Y. Gueguen (2009), Acoustic emissions monitoring during inelastic deformation of porous sandstone: Comparison of three modes of deformation, *Pure Appl. Geophys.*, *166*, 823–841, doi:10.1007/s00024-009-0479-0.

Freed, A. M. (2005), Earthquake triggering by static, dynamic and postseismic stress transfer, *Annu. Rev. Earth Planet. Sci.*, *33*, 335–367, doi:10.1146/annurev.earth.33.092203.122505.

Hickman, S., R. Sibson, and R. Bruhn (1995), Introduction to special section: Mechanical involvement of fluids in faulting, *J. Geophys. Res.*, *100*, 12,831–12,840, doi:10.1029/95JB01121.

Hillis, R. (2000), Pore pressure/stress coupling and its applications for seismicity, *Explor. Geophys.*, *31*, 448–454, doi:10.1071/EG00448.

House, L. (1987), Locating microearthquakes induced by hydraulic fracturing in crystalline rocks, *Geophys. Res. Lett.*, *14*, 919–921, doi:10.1029/GL014i009p00919.

Kaiser, E. J. (1959), A study of acoustic phenomena in tensile test, doctoral thesis, Tech. Hochsch. Munchen, Munich, Germany.

Kilb, D., J. Gomberg, and P. Bodin (2002), Aftershock triggering by complete Coulomb stresses, *J. Geophys. Res.*, *107*(B4), 2060, doi:10.1029/2001JB000202.

King, G. C. P., R. S. Stein, and J. Lin (1994), Static stress changes and the triggering of earthquakes, *Bull. Seismol. Soc. Am.*, *84*, 935–953.

Kristiansen, T. G., O. Barkved, and P. D. Pattilo (2000), Use of passive seismic monitoring in well and casing design in the compacting and subsiding Valhall Field, North Sea, *Pap. 65134*, Soc. of Pet. Eng., Richardson, Tex.

Miller, S. A., C. Collettini, L. Chiaraluce, M. Cocco, M. Barchi, and B. J. P. Kaus (2004), Aftershocks driven by a high-pressure CO2 source at depth, *Nature*, *427*, 724–727, doi:10.1038/nature02251.

Mourgues, R., and P. R. Cobbold (2003), Some tectonic consequences of fluid overpressures and seepage forces as demonstrated by sandbox modelling, *Tectonophysics*, *376*, 75–97, doi:10.1016/S0040-1951(03)00348-2.

Parotidis, M., E. Rothert, and S. A. Shapiro (2003), Pore-pressure diffusion: A possible triggering mechanism for the earthquake swarms 2000 in Vogtland/NW371 Bohemia, central Europe, *Geophys. Res. Lett.*, *30*(20), 2075, doi:10.1029/2003GL018110.

Parotidis, M., S. A. Shapiro, and E. Rothert (2004), Back front of seismicity induced after termination of borehole fluid injection, *Geophys. Res. Lett.*, *31*, L02612, doi:10.1029/2003GL018987.

Paterson, M. S., and T.-F. Wong (2005), *Experimental Rock Deformation: The Brittle Field*, 346 pp., Springer, Berlin.

Rothert, E., and S. A. Shapiro (2007), Statistics of fracture strength and fluid-induced microseismicity, *J. Geophys. Res.*, *112*, B04309, doi:10.1029/2005JB003959.

Rozhko, A. Y. (2008), Benchmark for poroelastic and thermoelastic numerical codes, *Phys. Earth Planet. Inter.*, *171*, 170–176, doi:10.1016/j.pepi.2008.08.016.

Rozhko, A. Y. (2010), Unconfined compressive strength of partially saturated shales: The fracture mechanics approach, paper presented at Shale Workshop 2010, Eur. Assoc. of Geosci. and Eng., Nice, France.

Rozhko, A. Y., Y. Y. Podladchikov, and F. Renard (2007), Failure patterns caused by localized rise in pore-fluid overpressure and effective strength of rocks, *Geophys. Res. Lett.*, *34*, L22304, doi:10.1029/2007GL031696.

Rutledge, J. T., W. S. Phillips, and B. K. Schuessler (1998), Reservoir characterization using oil-production-induced microseismicity, Clinton County, Kentucky, *Tectonophysics*, *289*, 129–152, doi:10.1016/S0040-1951(97)00312-0.

Sangha, C. M., and R. K. Dhir (1975), Strength and deformation of rock subject to multiaxial compressive stresses, *Int. J. Rock Mech. Min. Sci. Geomech. Abstr.*, *12*, 277–282, doi:10.1016/0148-9062(75)91085-2.

Scholz, C. H. (1968), Microfracturing and the inelastic deformation of rock in compression, *J. Geophys. Res.*, *73*, 1417–1432, doi:10.1029/JB073i004p01417.

Segall, P., and S. Fitzgerald (1998), A note on induced stress changes in hydrocarbon and geothermal reservoirs, *Tectonophysics*, *289*, 117–128, doi:10.1016/S0040-1951(97)00311-9.

Shapiro, S. A., and C. Dinske (2009a), Scaling of seismicity induced by nonlinear fluid-rock interaction, *J. Geophys. Res.*, *114*, B09307, doi:10.1029/2008JB006145.

Shapiro, S. A., and C. Dinske (2009b), Fluid-induced seismicity: Pressure diffusion and hydraulic fracturing, *Geophys. Prospect.*, *57*, 301–310, doi:10.1111/j.1365-2478.2008.00770.x.

Shapiro, S. A., J. Kummerow, C. Dinske, G. Asch, E. Rothert, J. Erzinger, H.-J. Kümpel, and R. Kind (2006), Fluid induced seismicity guided by a continental fault: Injection experiment of 2004/2005 at the German Deep Drilling Site (KTB), *Geophys. Res. Lett.*, *33*, L01309, doi:10.1029/2005GL024659.

Steacy, S., J. Gomberg, and M. Cocco (2005), Introduction to special section: Stress transfer, earthquake triggering, and time-dependent seismic hazard, *J. Geophys. Res.*, *110*, B05S01, doi:10.1029/2005JB003692.

Stein, R. S. (1999), The role of stress transfer in earthquake triggering, *Nature*, *402*, 605–609, doi:10.1038/45144.

Timoshenko, S. P., and J. N. Goodier (1982), *Theory of Elasticity*, 608 pp., McGraw-Hill, New York.

Zoback, M. D., and H.-P. Harjes (1997), Injection-induced earthquakes and crustal stress at 9 km depth at the KTB deep drilling site, Germany, *J. Geophys. Res.*, *102*, 18,477–18,491, doi:10.1029/96JB02814.

A. Y. Rozhko, European Technical Centre, M-I SWACO (a Schlumberger Co.), Koppholen 23, 4067 Stavanger, Norway. (arozhko01@miswaco.slb.com)